

PNAS



1

2 **Supporting Information for**

3 **Geometrical frustration versus Kitaev interactions in $\text{BaCo}_2(\text{AsO}_4)_2$**

4 **Thomas Halloran, Félix Desrochers, Emily Z. Zhang, Tong Chen, Zhijun Xu, Barry Winn, M. K. Graves-Brook, M. B. Stone,**
5 **Alexander I. Kolesnikov, Yiming Qiu, Ruidan Zhong, Robert Cava, Yong Baek Kim, Collin Broholm**

6 ²To whom correspondence should be addressed. E-mail: rzhongsjtu.edu.cn

7 **This PDF file includes:**

8 Supporting text

9 Figs. S1 to S6

10 SI References

11 Supporting Information Text

12 Additional INS Measurements

13 An additional set of measurements were run on the SEQUOIA spectrometer that was not presented in the main text. This
 14 is because the information in this measurement overlaps with the HYSPEC measurement, which has significantly better
 15 energy resolution ($\Delta E_{SEQ} = 1.3$ meV, $\Delta E_{HYS} = 0.15$ meV at the elastic line). Magnetic elastic scattering in the honeycomb
 16 plane is shown in Fig. S1. The non-magnetic component is removed using a $T=15$ K measurement as a background. The
 17 six-fold symmetric magnetic Bragg peaks are seen around the Γ -point consistent with the magnetic ordering wavevector of
 18 $\vec{k}_c = (0.27, 0, -1.31)$.

19 The scattering as a function of energy transfer along the $(h00)$ direction is shown in Fig. S2. This measurement had a large
 20 non-magnetic background from the vertical field split coil magnet, so it is difficult to distinguish the finer details of the zero-field
 21 magnetic excitations reported in the main text. However, the main magnon branch may be observed in panel (a), with a very
 22 faint branch of excitations extending up to $\hbar\omega = 12.1(5)$ meV. This branch does not persist above T_N in the paramagnetic
 23 phase. This may be more clearly seen in cuts through these data as a function of energy transfer in both the ordered and
 24 paramagnetic phases, which are shown in Fig. S3. These data were unavailable in our HYSPEC measurement, as we could
 25 not measure energy transfers this high in our zero-field configuration. It should be noted that a significant non-magnetic
 26 background exists in the sample environment, making it difficult to separate the magnetic signal at high energies. At low
 27 energies, the same features may be seen as in the main text though with coarser resolution and higher background in Fig. S3.

28 For $T > T_N$, we present higher energy scattering in zero field in Fig. S2(b) as well as a short measurement on HYSPEC in
 29 Fig. S4. These two measurements are not exactly the same, as the SEQ measurement is at $T=15$ K, and the HYS measurement
 30 is much closer to the ordering temperature at $T=6$ K. Both show that a gapless magnetic excitation spectrum persists far above
 31 the ordering temperature, extending to energies of $\hbar\omega = 2.5(2)$ meV. The momentum transfer dependence of the scattering
 32 cannot be accounted for by the magnetic form factor of Co^{2+} , and again confirms that strong dynamic correlations between
 33 spins persist above the ordering temperature.

34 Mapping between the crystallographic and Kitaev frames

The XXZ- J_1 - J_3 model can be related to the $JK\Gamma\Gamma'$ model by rotating the CF to the KF. Written in the KF, the local basis
 vectors of the CF are given by

$$\hat{x} = \frac{1}{\sqrt{6}} (1, 1, -2)^T \quad [1a]$$

$$\hat{y} = \frac{1}{\sqrt{2}} (-1, 1, 0)^T \quad [1b]$$

$$\hat{z} = \frac{1}{\sqrt{3}} (1, 1, 1)^T \quad [1c]$$

It follows that the spins written in the CF and the KF are related by the following transformation

$$\mathcal{U} = \begin{pmatrix} \frac{1}{\sqrt{6}} & -\frac{1}{\sqrt{2}} & \frac{1}{\sqrt{3}} \\ \frac{1}{\sqrt{6}} & \frac{1}{\sqrt{2}} & \frac{1}{\sqrt{3}} \\ -\sqrt{\frac{2}{3}} & 0 & \frac{1}{\sqrt{3}} \end{pmatrix}. \quad [2]$$

The local exchange matrices are accordingly mapped from the CF to the KF by

$$H_{\text{KF},\gamma}^{(i)} = \mathcal{U} H_{\text{CF},\gamma}^{(i)} \mathcal{U}^T. \quad [3]$$

Mapping general bilinear couplings on the nearest-neighbor z bond in the CF of the form

$$H_{\text{CF},z}^{(1)} = \begin{pmatrix} J_{xy}^{(1)} + D & E & F \\ E & J_{xy}^{(1)} - D & G \\ F & G & J_z^{(1)} \end{pmatrix} \quad [4]$$

to the KF, we obtain the exchange matrix

$$H_{\text{KF},z}^{(1)} = \begin{pmatrix} J + \eta & \Gamma & \Gamma'_1 \\ \Gamma & J - \eta & \Gamma'_2 \\ \Gamma'_1 & \Gamma'_2 & J + K \end{pmatrix} \quad [5]$$

with the following identification

$$J = -\frac{D}{3} + \frac{\sqrt{2}F}{3} + \frac{2J_{xy}^{(1)}}{3} + \frac{J_z^{(1)}}{3} \quad [6a]$$

$$\eta = -\frac{E}{\sqrt{3}} - \sqrt{\frac{2}{3}}G \quad [6b]$$

$$\Gamma = \frac{2D}{3} + \frac{\sqrt{2}F}{3} - \frac{J_{xy}^{(1)}}{3} + \frac{J_z^{(1)}}{3} \quad [6c]$$

$$\Gamma'_1 = -\frac{D}{3} + \frac{E}{\sqrt{3}} - \frac{F}{3\sqrt{2}} - \frac{G}{\sqrt{6}} - \frac{J_{xy}^{(1)}}{3} + \frac{J_z^{(1)}}{3} \quad [6d]$$

$$\Gamma'_2 = -\frac{D}{3} - \frac{E}{\sqrt{3}} - \frac{F}{3\sqrt{2}} + \frac{G}{\sqrt{6}} - \frac{J_{xy}^{(1)}}{3} + \frac{J_z^{(1)}}{3} \quad [6e]$$

$$K = D - \sqrt{2}F. \quad [6f]$$

We may write an equivalent conversion from the KF to the CF

$$J_{xy}^{(1)} = \frac{1}{3}(-\Gamma - \Gamma'_1 - \Gamma'_2 + 3J + K) \quad [7a]$$

$$J_z^{(1)} = \frac{1}{3}(2\Gamma + 2\Gamma'_1 + 2\Gamma'_2 + 3J + K) \quad [7b]$$

$$D = \frac{1}{3}(2\Gamma - \Gamma'_1 - \Gamma'_2 + K) \quad [7c]$$

$$E = \frac{\sqrt{3}}{8}(3\Gamma'_1 - 3\Gamma'_2 - 2\eta) \quad [7d]$$

$$F = \frac{\sqrt{2}}{6}(2\Gamma - \Gamma'_1 - \Gamma'_2 - 2K) \quad [7e]$$

$$G = \frac{\sqrt{6}}{8}(-\Gamma'_1 + \Gamma'_2 - 2\eta). \quad [7f]$$

35 It should be noted that assuming ideal edge-sharing bonds with C_{2v} symmetry, the NN couplings in the KF of Eq. (5) are
 36 constrained to $\eta = 0$ and $\Gamma'_1 = \Gamma'_2$. These constraints translate to $E = G = 0$ for the couplings in the CF of Eq. (4). The $R\bar{3}$
 37 spacegroup associated with BCO does break the C_{2v} symmetry for the nearest-neighbor bond. Co occupies the 6c Wyckoff
 38 site at $(00z)$ where $z = 0.17014(1)$. This corresponds to a puckering of Co in and out of the honeycomb plane by a distance
 39 $\pm(z - \frac{1}{6})c = 0.082\text{\AA}$.

The values in Eq. (14) of the main text are then represented in the KF by the following

$$J^{(1)} = -5.5 \text{ meV}, \quad [8a]$$

$$K^{(1)} = 0.1 \text{ meV}, \quad [8b]$$

$$\eta^{(1)} = 0.06 \text{ meV}, \quad [8c]$$

$$\Gamma^{(1)} = 2.2 \text{ meV}, \quad [8d]$$

$$\Gamma'_1^{(1)} = 2.0 \text{ meV} \quad [8e]$$

$$\Gamma'_2^{(1)} = 2.2 \text{ meV} \quad [8f]$$

$$J^{(3)} = 1.38 \text{ meV}, \quad [8g]$$

$$K^{(3)} = 0.0 \text{ meV}, \quad [8h]$$

$$\eta^{(3)} = 0.0 \text{ meV}, \quad [8i]$$

$$\Gamma^{(3)} = -1.2 \text{ meV}, \quad [8j]$$

$$\Gamma'_1^{(3)} = -1.2 \text{ meV}, \quad [8k]$$

$$\Gamma'_2^{(3)} = -1.2 \text{ meV}. \quad [8l]$$

Here, the superscripts denote the NN and third NN bonds. Equivalently, the set of test parameters in Eq. (15) in the main text

may be written in the CF as

$$J_{xy}^{(1)} = -5.0 \text{ meV}, \quad [9a]$$

$$J_z^{(1)} = -2.0 \text{ meV}, \quad [9b]$$

$$D = -3.5 \text{ meV}, \quad [9c]$$

$$E = 0 \text{ meV}, \quad [9d]$$

$$F = 8.1 \text{ meV}, \quad [9e]$$

$$G = 0 \text{ meV}. \quad [9f]$$

40 Molecular Dynamics

We first use finite temperature Monte Carlo (MC) techniques to obtain the spin configurations needed to compute the spin correlations. We treat the spins classically, i.e. we treat the spins as vectors $\mathbf{S} = (S_x, S_y, S_z)$ and we fix the magnitude to be $S = 1/2$. We use parallel tempering to first thermalize the system to the desired temperature for at least 5×10^6 MC sweeps. Then, we perform another 5×10^6 MC sweeps, with measurements recorded every 500 sweeps. The spin configurations are then used as initial configurations (IC) for molecular dynamics (MD)(2, 3), where each independent configuration is time-evolved deterministically according to the semi-classical Landau-Lifshitz-Gilbert equations of motion (4),

$$\frac{d}{dt} \mathbf{S}_i = -\mathbf{S}_i \times \frac{\partial H}{\partial \mathbf{S}_i}. \quad [10]$$

41 We allow the system to evolve for a long but finite time of $t = 300 \text{ meV}^{-1}$, with step sizes of $\delta t = 0.08 \text{ meV}^{-1}$ to obtain
 42 $S_i^\mu(t)S_j^\nu(0)$. We then average over all the ICs to obtain $\langle S_i^\mu(t)S_j^\nu(0) \rangle$. These results are then numerically Fourier transformed
 43 to obtain the momentum- and energy-dependent dynamical structure factors, $\mathcal{S}(\mathbf{q}, \omega)$. Our classical results are lastly re-scaled
 44 by a factor of $\beta\omega$, where $\beta = 1/k_B T$, in order to reflect the classical-quantum correspondence $\mathcal{S}_{\text{classical}}(\mathbf{q}, \omega) = \beta\omega \mathcal{S}_{\text{quantum}}(\mathbf{q}, \omega)$
 45 in the linear spin-wave theory framework (2).

46 Temperature Dependence of Magnetization Curves obtained by finite temperature Monte Carlo

47 In the main text, we present representative magnetization curves calculated by Monte Carlo for both the $JK\Gamma\Gamma'$ and $XXZ-J_1-J_3$
 48 models. The magnetization curves are presented for different temperatures: the $JK\Gamma\Gamma'$ model at $T=10^{-6}$ K, and the $XXZ-J_1-J_3$
 49 model at $T = 0.695$ K. For completeness we present magnetization curves calculated for both models at different temperatures
 50 and in-plane field angles in Fig. S6. As may be seen, for intermediate temperatures ($1.40 \text{ K} > T > 0.40 \text{ K}$), the $XXZ-J_1-J_3$ model
 51 can reproduce the two plateaus observed in experiments. As such, we have reported in the main text the result which most
 52 clearly reproduces the experimentally observed quantities. The high field magnetization response is approximately isotropic
 53 within the honeycomb plane at all temperatures.

54 In contrast, the $JK\Gamma\Gamma'$ model shows strong anisotropy versus the in-plane field angle at low temperatures. At higher
 55 temperatures saturation requires fields beyond 5 T. None of these latter curves are consistent the magnetization data for
 56 B CAO.

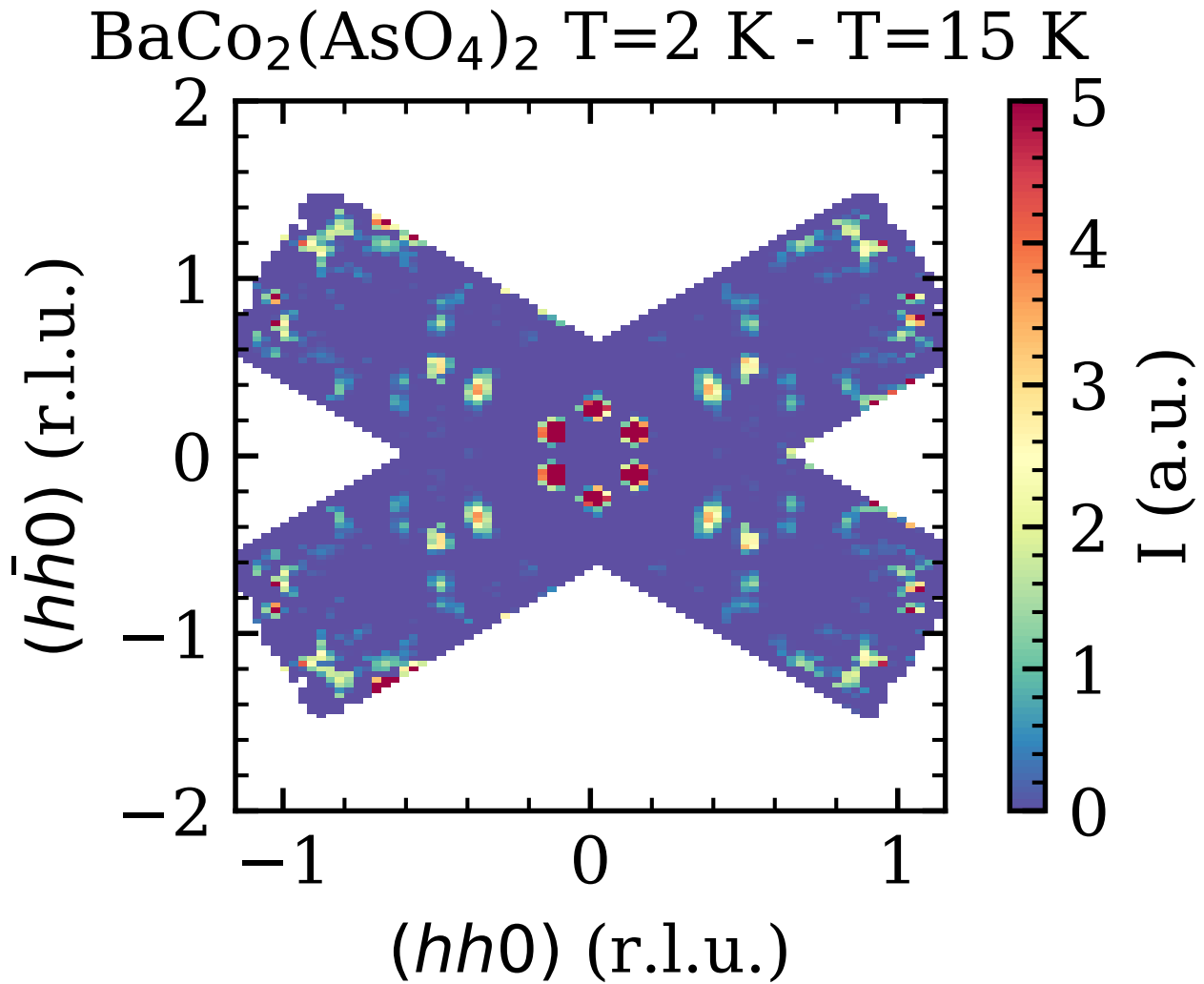


Fig. S1. Elastic magnetic neutron scattering from BaCo₂(AsO₄)₂ for wave vector transfer in the $(hk0)$ honeycomb plane acquired on the SEQUOIA instrument at ORNL. A $T=15$ K data set was subtracted to remove the nonmagnetic background. Scattering was averaged along $(00l)$ the entire available direction in $(00l)$, and from $\hbar\omega=-2$ meV to 2 meV.

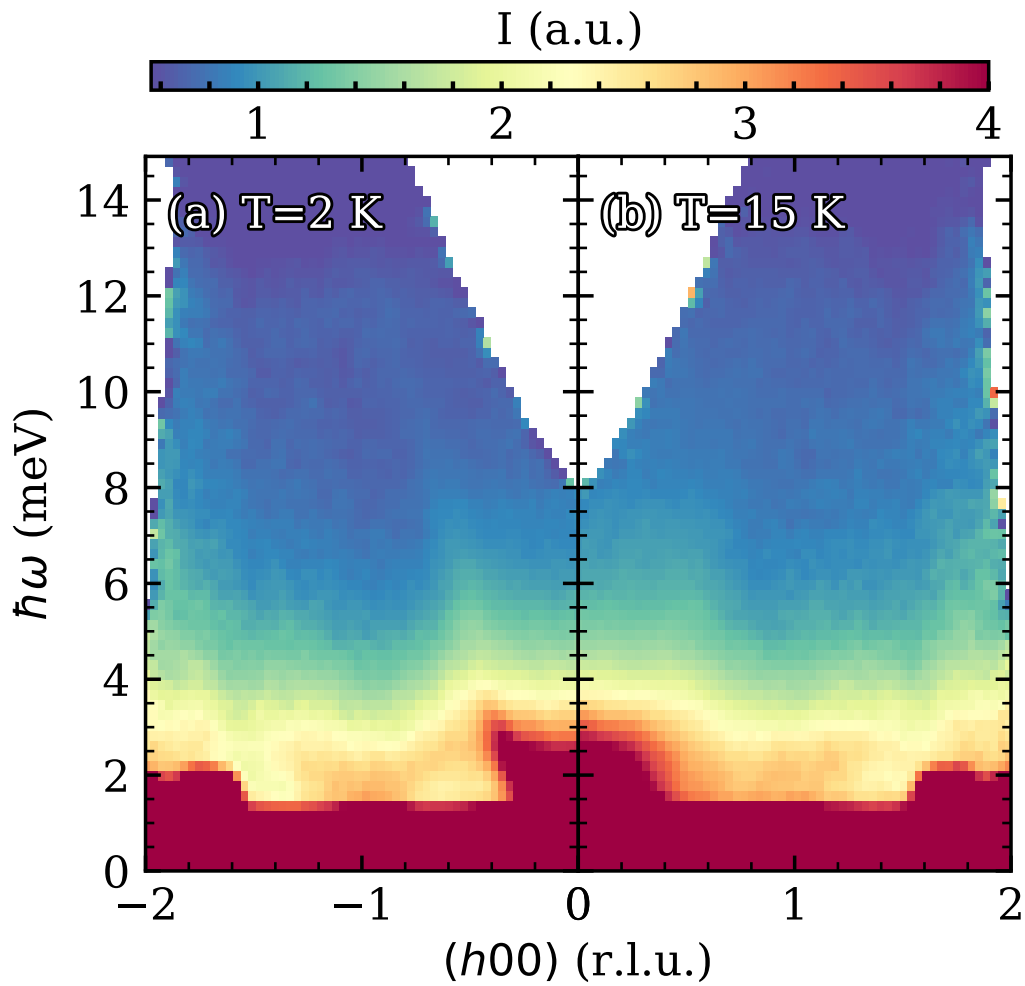


Fig. S2. Inelastic magnetic neutron scattering from $\text{BaCo}_2(\text{AsO}_4)_2$ versus energy $\hbar\omega$ and wave vector transfer along the $(h00)$ direction. (a) shows data from the long range ordered state $T < T_N$ while (b) shows data from the paramagnetic phase. The data were acquired on the SEQUOIA instrument at ORNL. Intensity for $\hbar\omega < 1.5$ meV is elastic scattering broadened by the instrumental resolution. Scattering was averaged over the full available $(00l)$ direction and from $k=-0.2$ to 0.2 .

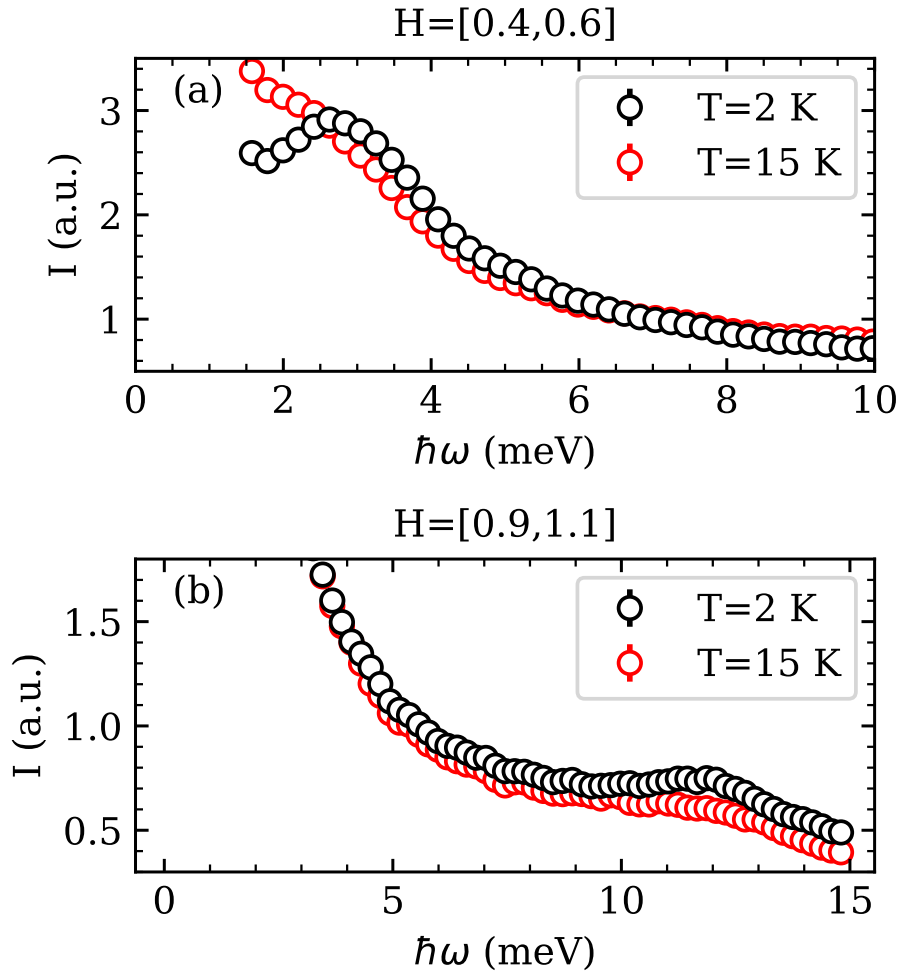


Fig. S3. Inelastic magnetic neutron scattering from $\text{BaCo}_2(\text{AsO}_4)_2$. $\hbar\omega$ -Cuts through the data in Fig. S2 are shown with wave vector transfer centered at $(\frac{1}{2}00)$ and (100) for frames (a) and (b) respectively. In (a) the emergence of a finite energy maximum is apparent for $T = 2$ K. (b) shows the presence of the $\hbar\omega=12$ meV Γ -point mode in the ordered state that is also apparent in Fig. 4(e) of the main paper. The averaging window in both plots along the $(0k0)$ direction is from $k = -0.2$ to $k = 0.2$, and the scattering is averaged across all available data in the $(00l)$ direction.

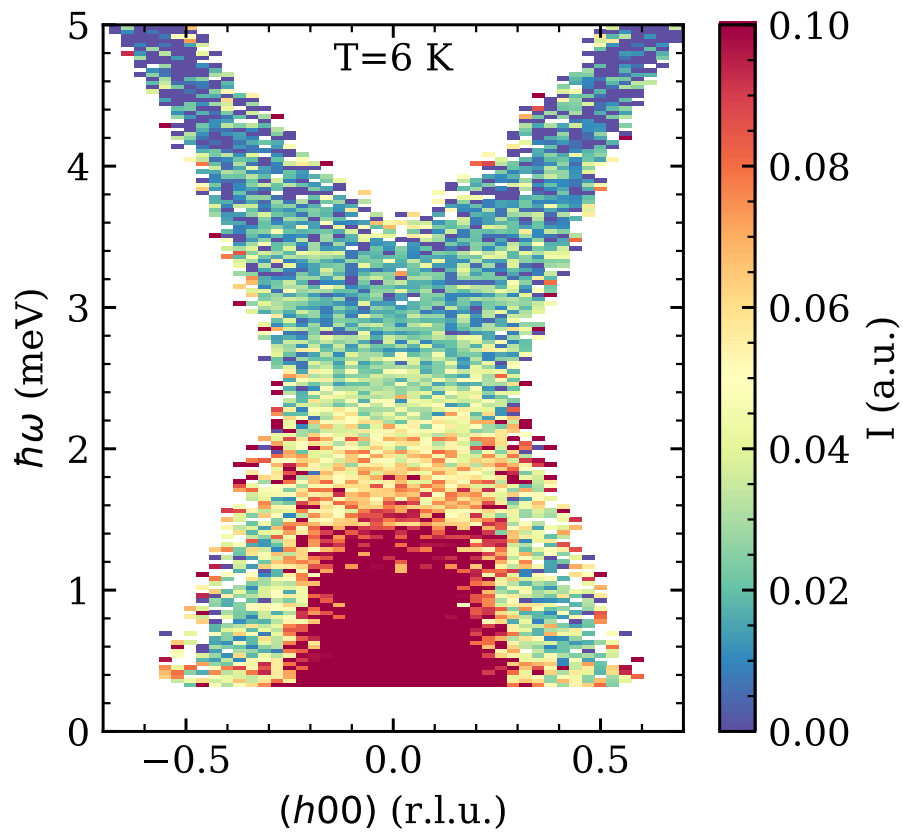


Fig. S4. Inelastic magnetic neutron scattering from $\text{BaCo}_2(\text{AsO}_4)_2$ acquired at $T = 6$ K, just above the ordering temperature on the HYSPEC instrument at ORNL. A broad continuum of scattering extends up to $\hbar\omega \approx 2.5$ meV indicating strong dynamic spin correlations in the paramagnetic phase of this frustrated quasi-two-dimensional quantum magnet. Scattering was averaged along the full available perpendicular $(h\bar{h}0)$ direction.

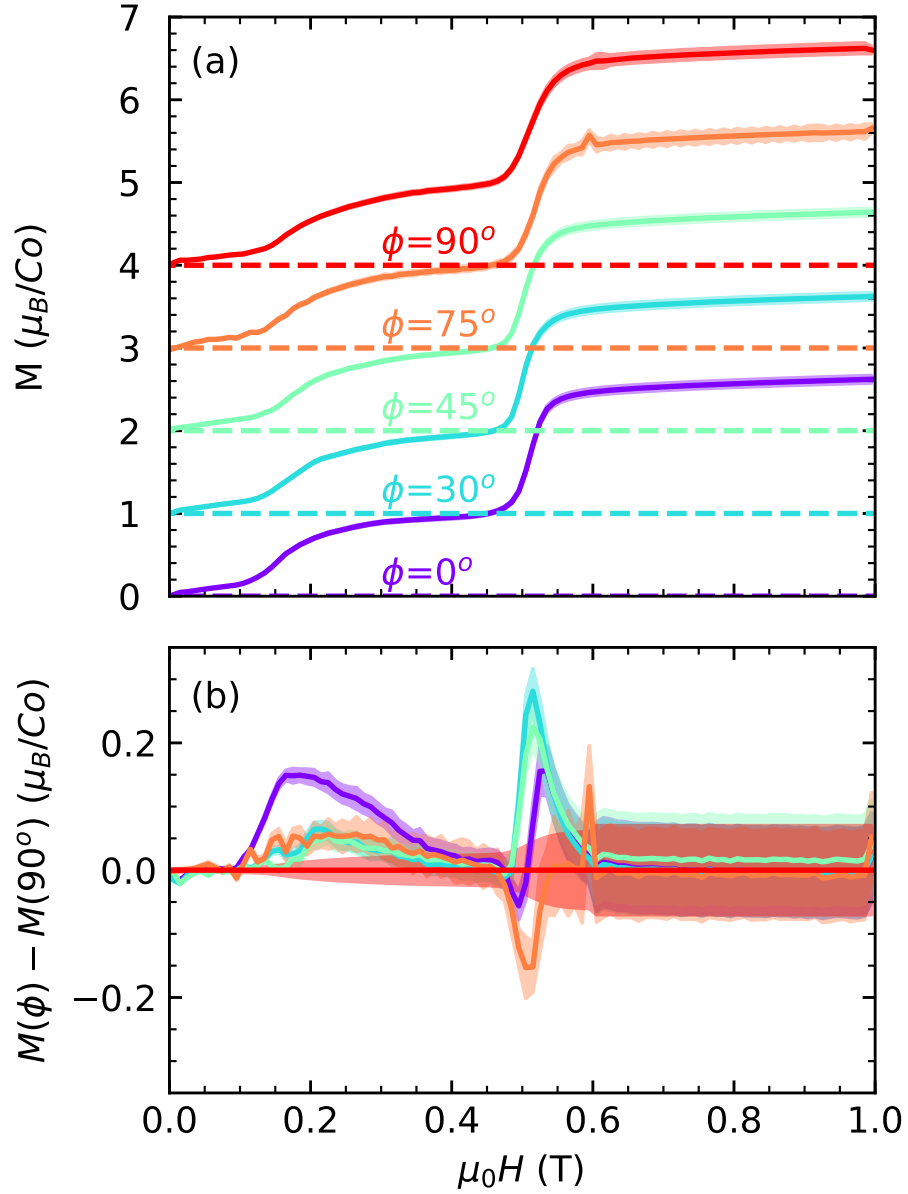


Fig. S5. Magnetization measurements for $\text{BaCo}_2(\text{AsO}_4)_2$ collected as a function in in-plane field angle with $\phi = 0^\circ$ corresponding to the $(1\bar{1}0)$ direction. Raw curves in (a) are shifted for each field angle for visual clarity, with the dotted lines showing the true zero for each ϕ . A difference plot using the $\phi = 90^\circ$ measurement as background is shown in (b) to make the subtle magnetization anisotropy apparent. In all plots, the shaded region corresponds to the instrumental error.

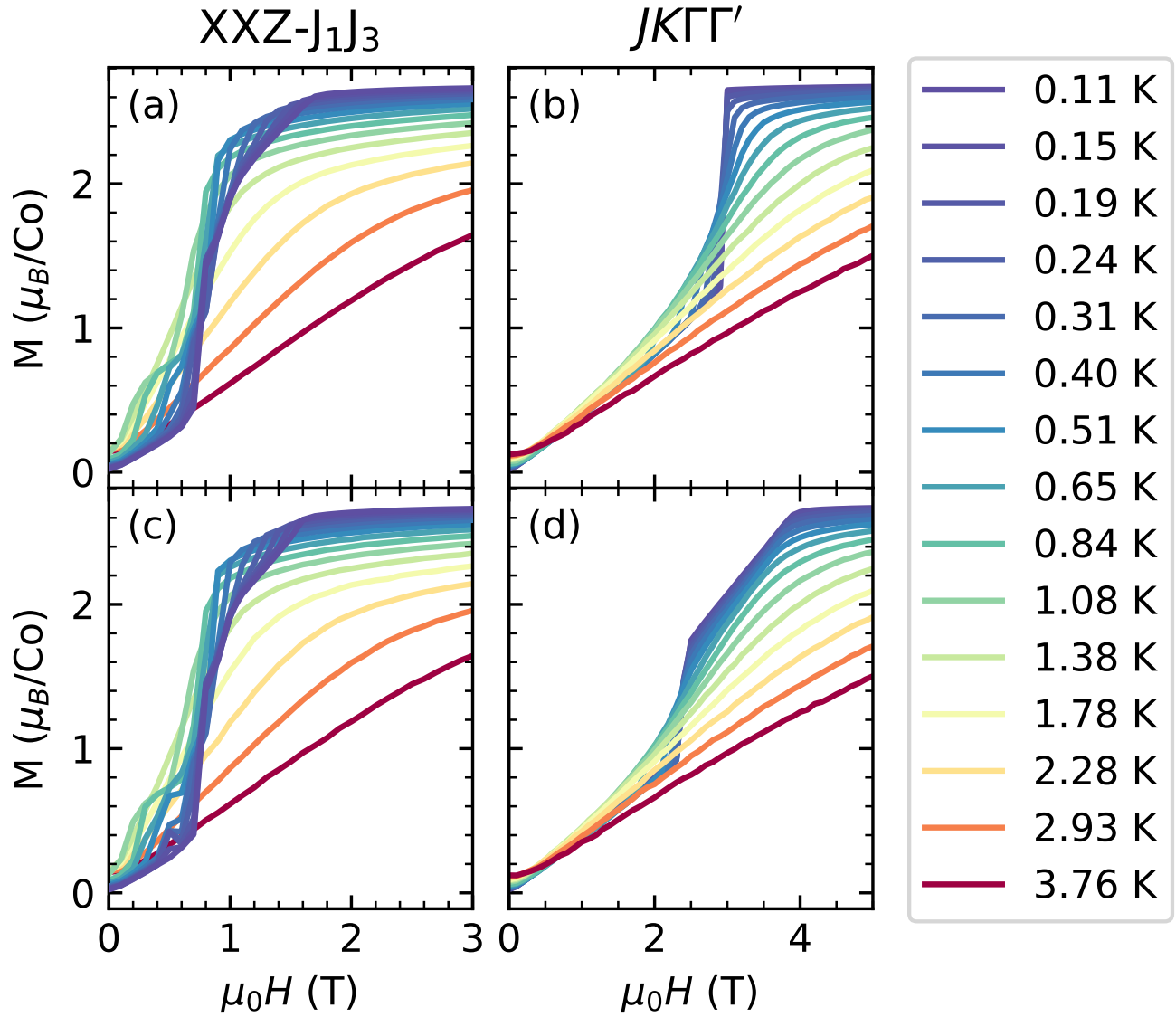


Fig. S6. Magnetization curves computed by finite temperature Monte Carlo for the $XXZ-J_1J_3$ model ((a) and (c)), and for the $JK\Gamma\Gamma'$ model ((b) and (c)) with the set of exchange parameters presented in the main text. For both models the magnetization curves are presented for a field along the \hat{x} -axis (a-b) and \hat{y} -axis (c-d) as defined in Fig. 1 of the main text.

57 **References**

- 58 1. R Zhong, T Gao, NP Ong, RJ Cava, Weak-field induced nonmagnetic state in a Co-based honeycomb. *Sci. Adv.* **6** (2020).
59 2. S Zhang, HJ Changlani, KW Plumb, O Tchernyshyov, R Moessner, Dynamical structure factor of the three-dimensional
60 quantum spin liquid candidate NaCaNi₂F₇. *Phys. Rev. Lett.* **122**, 167203 (2019).
61 3. R Moessner, JT Chalker, Properties of a classical spin liquid: the heisenberg pyrochlore antiferromagnet. *Phys. review*
62 *letters* **80**, 2929 (1998).
63 4. M Lakshmanan, The fascinating world of the landau–lifshitz–gilbert equation: an overview. *Philos. Transactions Royal Soc.*
64 *A: Math. Phys. Eng. Sci.* **369**, 1280–1300 (2011).